

PHOTOEVAPORATION OF PROTOSTELLAR DISKS V. CIRCUMSTELLAR DISKS UNDER THE INFLUENCE OF BOTH EUV AND FUV RADIATION

Sabine Richling^{1,2} and Harold W. Yorke^{2,1}

¹*Astronomisches Institut, Am Hubland, D-97074 Würzburg, Germany*

²*MS 169-506, Jet Propulsion Laboratory, California Institute of Technology, Pasadena, CA 91109*

ABSTRACT

The evolution and appearance of protostellar disks can be significantly altered by their UV environment. We investigate numerically the photoevaporation of protostellar disks under the influence of an external radiation field with both EUV ($h\nu > 13.6$ eV) and FUV ($6 \text{ eV} < h\nu < 13.6$ eV) components. Our 2D axisymmetric radiation hydrodynamics calculations begin with star-disk configurations resulting from previously published collapse simulations. We follow the evolution after the external UV radiation source has been turned on. We consider the transfer of both direct (from the UV point source) as well as diffuse radiation fields simultaneously with the ionization of hydrogen and carbon. A simplified cooling function is employed which assumes that the carbon ionization front separates the molecular region from the region in atomic or ionized form. For some simulations an isotropic stellar wind has been included at the position of the disk's central star. At selected evolutionary times a frequency-dependent ray-tracing diagnostic code is used to calculate emission line spectra and emission line maps over the volume of interest.

The interaction of the FUV-induced neutral flow at the disk surface with the direct and diffuse EUV radiation fields leads to the typical head-tail objects with bright emission line crescents and tails pointing away from the external radiation source. The properties of the head-tail objects are in agreement with the properties of the proplyds in the Orion Nebula, M8, NGC 2024, and — in a more extreme UV environment — of the newly discovered proplyds in NGC 3603. After losing material via photoevaporation over a time $\gtrsim 10^5$ yr, our initially rather massive disks are reduced to typical observed disk masses. At this time the radius of the disk, the radius of the hydrogen ionization front, and the length of the tail are compatible to observed proplyds. Our model disks can be either silhouetted or non-silhouetted in the emission line maps, depending on orientation. The [OIII] 5007 Å emission appears diffuser than [OII] 3726 Å, because the abundance of OIII is low near the hydrogen ionization front and in the shadow regions along the tail. Monopolar and bipolar micro-jets emerging from the proplyds can be explained by spherically symmetric stellar winds hydrodynamically focused by the neutral evaporating flow from the disk surface.

Subject headings: hydrodynamics - radiation transfer - stars: formation - circumstellar disks - HII regions - line: formation

1. Introduction

The occurrence of disks around young stars and protostars is a common feature in star forming regions. Circumstellar disks are detected by direct imaging around low-mass (Padgett et al. 1999), intermediate-mass (Mannings & Sargent 1999), and high-mass stars (Cesaroni et al. 1999), in binary systems (Close et al. 1998, Stapelfeldt et al. 1998), and in more evolved gas-poor or gas-less stages (Körner et al. 1998). Circumstellar disks are continually evolving; the principal dispersal mechanism is attributed to photoevaporation by ultraviolet radiation (Hollenbach, Yorke & Johnstone 2000). Whereas disks of high-mass stars are photoevaporated by the central star, disks of young low-mass stars are subject to photoevaporation by nearby massive stars and/or to some extent by their own X-rays from hot coronae.

Examples for externally ionized protostellar disks are the well studied objects in the Orion Nebula (O’Dell, Wen & Hu 1993; McCaughrean & Stauffer 1994; Chen et al. 1998; Bally et al. 1998a). These objects, commonly referred to as proplyds (PROto-PLANetary DiskS), are often interpreted as the ionized envelopes of young star-disk systems. In optical emission lines ($H\alpha$, [OIII], [NII]) they appear as bright heads with tails pointing away from the major ionizing source θ^1 Ori C. Some of them contain dark silhouettes which match the [OI] and H_2 emission and probably trace the surface of an embedded optically thick disk. Infrared images show the presence of central stars in most of the proplyds. The detection of similar objects in M8 (Stecklum et al. 1998), NGC 3603 (Brandner et al. 1999), and NGC 2024 (Stapelfeldt et al. 1999) suggests that photoevaporation by an external star is an important process for the evolution of circumstellar disks.

The appearance of proplyds can be explained by the interaction of EUV ($h\nu > 13.6$ eV) and FUV (6 eV $< h\nu < 13.6$ eV) radiation from an external source with the circumstellar disk. FUV photons are absorbed principally by dust. They reach the surface of the disk, dissociate the molecules, heat the neutral material, and create a neutral flow of warmed disk material. EUV photons are mostly absorbed by ionization of neutral hydrogen and are prevented from reaching the disk surface by the neutral flow. Thus, the ionization front stands off at a distance from the disk surface, appearing as a bright round head in the direction of the illuminating source and containing a

disk embedded in a warm photon-dominated or photodissociation region (PDR). The tail traces the confined part of the ionization front at the back side of the disk.

Johnstone, Hollenbach & Bally (1998) presented analytical and numerical models for the structure of such neutral flows. Depending on the radius of the disk, the flux of EUV and FUV photons and the column of neutral gas in the PDR, the neutral flow can either be EUV-dominated or FUV-dominated. In EUV-dominated flows the PDR is very thin and the flux of EUV photons determines the mass loss rate. In FUV-dominated regions the PDR consists of a supersonic wind region and a thick subsonic layer separated by a shock front. The mass loss rate is determined by the FUV photon flux. Störzer & Hollenbach (1999) improved these models by including the results of equilibrium and non-equilibrium PDR codes to calculate the column density and temperature inside the PDR. They determined under which circumstances FUV-dominated flows are possible and conclude that the observed sizes of the ionization fronts of many proplyds in the Orion Nebula can be explained by FUV-dominated flows. From the resulting mass loss rates, an assumed surface density distribution and an illumination time scale equal the age of the Orion star forming region ($10^5 - 10^6$ yr, Hillenbrand 1997) they calculate disk masses which are consistent with the observed disk masses ($< 0.02 M_\odot$, Bally et al. 1998b).

The models of Johnstone et al. (1998) and Störzer & Hollenbach (1999) assume a steady-state spherical flow emerging from a spherical clump and do not determine the density and flow structure self-consistently with the thermal structure and the radiation field. By contrast, we use a fully self-consistent 2D radiation hydrodynamics code and follow the evolution of a star-disk system after an external UV radiation source has switched on. Due to the two-dimensional setup and a proper treatment of diffuse radiation fields it is possible to examine the photoevaporation flow at the top, the edge, and the back side of the disk, a probable redirection of material from the head into the tail and the evolution of the disk and the tail itself. Shocks appear as a natural consequence of the interacting flows. A ray-tracing procedure is used to calculate maps for various emission lines allowing a demonstrative comparison with observations. This work is a continuation of our previous work, where only the EUV radiation was considered (Richling &

Yorke 1998). Here, we present the results obtained with an extended code which includes the effects of FUV radiation via a simplified PDR model.

In section 2 we give a short introduction to the radiation hydrodynamics code. In the section 3 we present the PDR model and describe the necessary modifications to the code. The star-disk models and the parameters of the calculations are described in section 4. In section 5 and 6 we present the results of the radiation hydrodynamical simulations and of the diagnostic ray-tracing code. Finally, we give a summary of our results in section 7.

2. The radiation hydrodynamics code

Many features of the physical model and the numerical procedures used in the 2D radiation hydrodynamics code are described in the previous papers of this series (Yorke & Welz 1996, Richling & Yorke 1997, Richling & Yorke 1998). The code solves the hydrodynamical equations in cylindrical coordinates on self-similar nested grids (Yorke & Kaisig 1995). This allows us to numerically resolve the disk well, especially close to the central star, while covering a large volume of space. Self-gravity and an α -viscosity (Shakura & Sunyaev 1973) are included. The transfer of EUV and FUV photons is calculated along lines of sight centered at the star outside the computational domain. The external UV source is freely relocatable along the rotation axis of the system. The dust temperature is determined by a continuum radiation transfer module which employs the grey flux-limited diffusion (FLD) approximation (Levermore & Pomraning 1981, Yorke & Kaisig 1995). The FLD approximation is also used to calculate the three diffuse UV radiations fields: soft EUV photons ($h\nu \sim 14$ eV), resulting from recombinations of hydrogen into the ground state, and EUV as well as FUV photons, resulting from scattering on dust grains. The most important heating and cooling contributions in HII regions and PDRs are considered. In the following we describe the FUV related physics in detail.

3. The PDR model

PDRs contain all of the atomic and most of the molecular gas and are often modeled analytically and numerically (see e.g. review by Hollenbach & Tielens 1997). One-dimensional models usually consider complex chemical networks to calculate the temperature structure and the abundances of various atomic

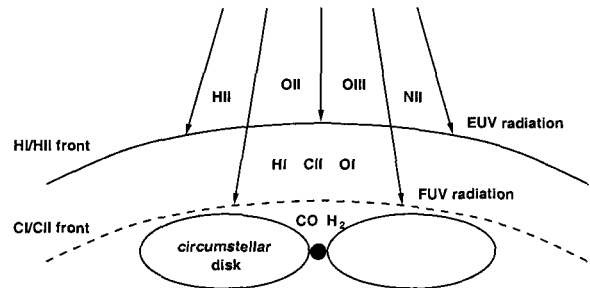


Fig. 1.— The PDR-model. A circumstellar disk is illuminated by EUV photons ($h\nu > 13.6$ eV) and FUV photons ($6 \text{ eV} < h\nu < 13.6$ eV). EUV photons ionize hydrogen until they reach the H I-front. FUV photons penetrate the H I-front and reach the C I-front close to the disk surface. Our models assume that the material is molecular behind the C I-front and atomic or ionized (depending on the ionization potential) between the C I-front and the H I-front.

and molecular species. In 2D simulations including radiation transfer it would be far too time-consuming to include such elaborate chemical networks. Consequently, some simplifying assumptions must be made.

Our PDR model is shown schematically in Figure 1. A circumstellar disk is illuminated by EUV and FUV photons. EUV photons ionize hydrogen until they reach the hydrogen ionization front (H I-front). The HII region is heated principally by the excess energy of electrons ejected during photoionization of hydrogen and cooled by forbidden line radiation of NII, OII, and OIII. FUV photons penetrate deeper into the medium until they reach the carbon ionization front (C I-front). We assume that between the H and C I-fronts the material consists of atomic hydrogen and singly ionized “metals” with ionization potentials below 13.6 eV. Behind the C I-front the material is molecular, i.e., the C I-front and the dissociation fronts are assumed to coincide. Within the PDR the major heating mechanism is photoejection of electrons from dust grains; the gas is cooled by fine-structure line emission of OI and CII.

This approximation is well justified for the current problem. The gas density at the border of the disk increases by about two orders of magnitude within 3–4 grid cells. The C I-front lies exactly within this region and has approximately the same width. Plane-parallel models for dense equilibrium PDRs (Sternberg & Dalgrano 1995) and non-equilibrium PDRs

(Störzer & Hollenbach 1998) show that the C I-front and the dissociation fronts of H_2 and CO are usually co-located within a column density of about one order of magnitude. We thus expect that these fronts practically coincide within the limited resolution of our numerical grid. The large drop of the temperature behind the C I-front is another plausible reason to use it as the boundary between the warm PDR gas and the cool disk material (Johnstone & Bertoldi 1998). Of course, certain species appear predominantly in narrow zones between the C I-front and the dissociation fronts. Thus, a more careful treatment — beyond the scope of the present investigation — would be necessary to resolve the emission features of these species.

3.1. UV photon rates

The EUV and FUV photon rates S_{EUV} and S_{FUV} of the external radiation source are estimated from an assumed luminosity L and effective temperature T_{eff} :

$$S_{\text{EUV}} = \frac{\int_{\nu_{\text{EUV}}}^{\infty} B_{\nu}(T_{\text{eff}})/h\nu d\nu}{\int_0^{\infty} B_{\nu}(T_{\text{eff}}) d\nu} \times L, \quad (1)$$

$$S_{\text{FUV}} = \frac{\int_{\nu_{\text{FUV}}}^{\nu_{\text{EUV}}} B_{\nu}(T_{\text{eff}})/h\nu d\nu}{\int_0^{\infty} B_{\nu}(T_{\text{eff}}) d\nu} \times L \times \gamma, \quad (2)$$

where B_{ν} is the Planck function, $h\nu_{\text{EUV}} = 13.6$ eV and $h\nu_{\text{FUV}} = 6$ eV. The three parameters L , T_{eff} and the dimensionless factor γ in equation 2 allow us to vary the magnitude, hardness, and FUV/EUV ratio of the UV photon rates independently in order to investigate parameter space.

3.2. Transfer of direct FUV photons

The FUV photon density $u_{\text{direct}}^{\text{FUV}}$ from direct stellar illumination is calculated along lines of sight centered at the external source by solving the equation

$$u_{\text{direct}}^{\text{FUV}} = \frac{S_{\text{FUV}}}{4\pi d^2 c} \exp(-\tau_{\text{FUV}}) \quad (3)$$

with the FUV optical depth

$$\tau_{\text{FUV}} = \int [n_{\text{C}}(1 - x_{\text{C}})\sigma_{\text{C}}^{\text{FUV}} + \kappa^{\text{ext}}] ds. \quad (4)$$

We consider extinction due to ionization of carbon and dust extinction. n_{C} is the particle density and x_{C} the degree of ionization of carbon. $\sigma_{\text{C}}^{\text{FUV}}$ is the photoionization cross section of carbon averaged over the FUV photon spectrum between 11.26 eV $< h\nu <$

13.6 eV. The dust extinction coefficient κ^{ext} depends on the abundance and the composition of the dust grains. Dust models (Draine & Lee 1984, Preibisch et al. 1993) propose values in the range of $\kappa^{\text{ext}}/\rho = 10^2 - 10^3$ cm² g⁻¹. In the vicinity of protostellar disks small grains should be depleted due to sedimentation, coagulation, and sputtering in shocks which leads to a lower FUV extinction coefficient (Suttner, Yorke & Lin 1999). We choose $\kappa^{\text{ext}}/\rho = 300$ cm² g⁻¹.

3.3. Diffuse FUV radiation

The diffuse FUV photon density $u = u_{\text{dust}}^{\text{FUV}}$ resulting from scattering on dust grains is determined by solving the flux-limited diffusion equation

$$\frac{\partial u}{\partial t} - \nabla \cdot \left(\frac{\lambda c}{\chi^{\text{ext}}} \nabla u \right) = \epsilon - \chi^{\text{abs}} c u, \quad (5)$$

where the flux-limiter λ is given by

$$\lambda = \frac{1}{R} \left(\coth R - \frac{1}{R} \right) \quad \text{with} \quad R = \frac{|\nabla u|}{\chi^{\text{ext}} u}. \quad (6)$$

Emission rate ϵ , extinction coefficient χ^{ext} and absorption coefficient χ^{abs} are calculated from

$$\epsilon = \kappa^{\text{scat}} c u_{\text{star}}^{\text{FUV}}, \quad (7)$$

$$\chi^{\text{ext}} = n_{\text{C}}(1 - x_{\text{C}})\sigma_{\text{C}}^{\text{FUV}} + \kappa^{\text{ext}}, \quad (8)$$

$$\chi^{\text{abs}} = n_{\text{C}}(1 - x_{\text{C}})\sigma_{\text{C}}^{\text{FUV}} + \kappa^{\text{abs}}. \quad (9)$$

We assume isotropic scattering and a dust scattering coefficient $\kappa^{\text{scat}}/\rho = 200$ cm² g⁻¹.

3.4. Ionization/recombination of carbon

The degree of ionization of carbon x_{C} is determined by solving the time-dependent rate equation

$$\frac{\partial x_{\text{C}}}{\partial t} = (1 - x_{\text{C}}) [\sigma_{\text{C}}^{\text{FUV}} u^{\text{FUV}} + \sigma_{\text{C}}^{\text{EUV}} u^{\text{EUV}}] c - \alpha_{\text{C}} x_{\text{C}} n_{\text{e}}. \quad (10)$$

Here, u^{EUV} and u^{FUV} are the sums of all direct and diffuse EUV and FUV photon densities. $\sigma_{\text{C}}^{\text{EUV}}$ is the photoionization cross section of carbon averaged over the EUV photon spectrum. The total recombination coefficient

$$\alpha_{\text{C}} = 3.74 \times 10^{-12} \left(\frac{T}{300 \text{ K}} \right)^{-0.5} \quad (11)$$

is taken from Bertoldi (1999). It is an approximation for gas temperatures between $T = 10 - 10^4$ K of the

results obtained by Nahar & Pradhan (1994), including both radiative and dielectronic recombination of carbon. The electron density $n_e = nx + n_C x_C$ consists of contributions from the ionization of hydrogen and carbon, where x is the degree of ionization of H and n the total particle density.

3.5. Heating

The major heating mechanism in PDRs is photoelectric ejection of electrons from grains. The corresponding heating function depends on composition, size distribution, and charge of the dust grains. Bakes & Tielens (1994) numerically determined a heating rate in dependence on the gas temperature T , the electron density n_e , and the FUV flux G_0 in Habing units ($H = 1.6 \times 10^3 \text{ erg cm}^{-2} \text{ s}^{-1}$) for $T_{\text{eff}} = 30\,000 \text{ K}$. We use their analytical approximation of the heating rate

$$\Gamma = 10^{-24} \eta G_0 n \text{ erg s}^{-1} \quad (12)$$

with the heating efficiency

$$\eta = \frac{3 \times 10^{-2}}{1 + 2 \times 10^{-4} T^{0.5} G_0 / n_e} \quad (13)$$

and the correction factor obtained by Spaans et al. (1994) for different T_{eff} .

3.6. Cooling

The cooling in PDRs is dominated by collisional excitation of fine structure lines. We consider the most important lines [CII] $158 \mu\text{m}$, [OI] $63 \mu\text{m}$, and [OI] $145 \mu\text{m}$ and use the escape probability formalism according to Tielens & Hollenbach (1985) to calculate the cooling rate of a transition from level i to level j

$$\Lambda = n_i A_{ij} h \nu_{ij} \beta_{\text{esc}}(\tau_{ij}), \quad (14)$$

where n_i is the population density of the upper level obtained by solving the corresponding rate equations. A_{ij} is the spontaneous transition probability and $h \nu_{ij}$ the energy difference between level i and j . The escape probability $\beta_{\text{esc}}(\tau_{ij})$ is calculated using a formula given by de Jong, Dalgarno & Boland (1980). The optical depth of the line τ_{ij} is determined by integrating along a different set of lines of sight as described in section 3.2. Here, the lines of sight start at the boundary cells of the numerical grid and are centered at the position of the star within the disk. Although the lines of sight are not always perpendicular to the

surface of the disk, this procedure should provide an approximation for τ_{ij} which is adequate for our purposes.

4. Initial conditions

4.1. Star-disk models

The starting models are circumstellar disk systems resulting from collapse simulations of 1 and 2 M_{\odot} molecular clumps (Yorke & Bodenheimer 1999). Since the collapse code employs the same numerical techniques, we are able to follow self-consistently the evolution of a low-mass system within a star-forming cluster. Switching on the external UV source means that the star-disk system either comes into contact with an existing HII region or is suddenly illuminated by a new-born massive star nearby.

The characteristic parameters of the models are summarized in Table 1. The luminosity L_{star} of the protostar with mass M_{star} is the sum of an intrinsic stellar luminosity and an accretion luminosity. The radius of the disk R_{disk} is defined by its sudden decrease in density of about two orders of magnitude and depends on the initial conditions of the parental molecular clump. Models I and III evolved from a rather extended molecular clump with a radius approximately equal to the extension of the coarsest grid X_{max} . Their disks have radii $R_{\text{disk}} \sim 10^3 \text{ AU}$. Model II evolved from a less extended molecular clump and has a disk with a much smaller radius ($R_{\text{disk}} = 180 \text{ AU}$) and with better spatial resolution within the innermost grid. The evolutionary age t_{disk} of the models is in the range of 2 to 3 free-fall times.

4.2. The calculations

The 2D simulations of the evolution of star-disk systems under the influence of EUV and FUV radiation require a huge amount of CPU time and depend on the choice of a large set of free parameters. Because it is impossible to examine this multidimensional parameter space fully, we used observationally related setups and varied some of the parameters in order to test their influence on the evolution.

Table 2 shows the parameters of the calculated cases. Simulations A to G examine the situation of the proplyds in the Orion Nebula: The EUV and FUV photon rates resemble those of the main ionizing source in the Trapezium Cluster. The distances d between the star-disk system and the external source are

Table 1: Circumstellar Disk Models (from Yorke & Bodenheimer 1999)

model	M_{star} M_{\odot}	L_{star} L_{\odot}	T_{dust}^c K	M_{disk} M_{\odot}	R_{disk} 1000 AU	t_{disk} 10^3 yr	$t_{\text{disk}}/t_{\text{ff}}$	numerical grid $N_G \times N_Z \times N_R$	X_{max} 1000 AU	ΔX_{min} AU
I	0.58	3.68	150	0.40	1.0	215	2.2	$4 \times 244 \times 122$	6.82	6.85
II	0.66	17.1	932	0.35	0.18	27.0	3.1	$5 \times 116 \times 58$	1.34	1.44
III	1.14	11.3	398	0.90	1.7	438	2.2	$6 \times 116 \times 58$	13.5	7.28

Note— M_{star} = mass of the central star; L_{star} = luminosity of the central star; T_{dust}^c = central dust temperature; M_{disk} = disk mass; R_{disk} = disk radius; t_{disk} = disk age in 10^3 yr and in free-fall times t_{ff} ; N_G = level of grid nesting; $N_Z \times N_R$ = number of cells per grid level; X_{max} = the extension of the coarsest grid in radial and $\pm Z$ directions; ΔX_{min} = resolution of the finest grid.

Table 2: Parameters for the Cases Calculated

case	model	d 10^{17} cm	L $10^6 L_{\odot}$	$\log S_{\text{EUV}}$ s^{-1}	$\log S_{\text{FUV}}$ s^{-1}	γ	$\log f_{\text{EUV}}$ $\text{cm}^{-2} \text{s}^{-1}$	$\log f_{\text{FUV}}$ $\text{cm}^{-2} \text{s}^{-1}$	v_{wind} km s^{-1}	$\log \alpha$
A	I	3.08	0.147	48.86	49.25	1	12.8	13.2	5	-6
B	I	1.54	0.147	48.86	49.25	1	13.4	13.8	5	-6
C	I	1.05	0.147	48.86	49.25	1	13.7	14.1	5	-6
D	I ^a	1.54	0.147	48.86	49.25	1	13.4	13.8	100	-6
E	I ^a	1.54	0.147	48.86	49.25	1	13.4	13.8	200	-6
F	II	1.54	0.147	48.86	49.25	1	13.4	13.8	5	-6
G	II	1.54	0.147	48.86	49.25	1	13.4	13.8	5	-2
H	III	40.1	20.2	51.00	51.38	1	12.7	13.1	5	-6
J	III	40.1	20.2	51.00	52.09	5	12.7	13.8	5	-6

Note— starting models from Tab. 1; d = distance of ionizing star from disk's center; L = luminosity of ionizing star; S = UV photon rates of ionizing star; γ = dimensionless FUV/EUV flux ratio (see equation 2); $f = S/4\pi d^2$ = photon fluxes at the disk's center; v_{wind} = velocity of the wind originating from the disk's central star; α = parameter for angular momentum transfer. The effective temperature is the same in all simulations $T_{\text{eff}} = 38\,500$ K.

^aSimulation starts with model I of case A at $t = 59.3 \times 10^3$ yr.

in the range of 0.1 and 0.025 pc which are typical values for the Orion proplyds (Bally et al. 1998a). Cases H and J simulate the evolution of star-disk system III illuminated by a cluster of O-stars and were originally intended to model the recently detected proplyds in NGC 3603 (Brandner et al. 1999). Since the photon fluxes at the disk's center are comparable to simulations A to G, the results of case H and J can also be applied to the Orion proplyds, except for the minor effect that the lines of sight are more nearly parallel at the disk's position. For the simulations with initial conditions I and III the calculations are stopped when the radial extent of the disk falls below 10 grid cells on the finest grid.

5. Results

5.1. General evolution (case A)

The evolution of star-disk system I in case A is displayed in Figure 2. The grey scale represents the density structure and the arrows show the velocity field. The black contour lines for the degree of ionization of hydrogen mark the position of the H I-front separating the hot ionized gas from the warm PDR material. The external radiation source is located at $d = 0.1$ pc above the disk. The upper left frame (Fig. 2a) shows the very early structure of the system: 10^2 yr after the sudden onset of the external radiation source the C I-front (white contour lines) already envelops the densest parts of the disk. FUV photons heat the gas to temperatures up to 5000 K and launch a neutral flow above the disk expanding with a supersonic velocity. The H I-front approaching from the top is still unaffected by the presence of the disk.

Approximately 10^3 yr later (Fig. 2b), diffuse FUV photons have established a neutral flow below the disk, and the disk is embedded in a wind-blown bubble of neutral gas. The bubble is confined by a shock front with a radius R_S which is about twice as large as the radius of the disk defined by the radius of the C I-front R_C . The disk itself is considerably disturbed at its outer edge. This phenomenon also occurred in our earlier simulations (Richling & Yorke 1998) which considered the effects of EUV only. Due to the asymmetrical EUV radiation field the disk was gradually truncated to a radius where the gas pressure in the disk compensates the external pressure. Here, the distortion is caused by the asymmetrical FUV radiation field. In Figure 2b the H I-front compresses the neutral flow beyond the bubble to a thick layer

of subsonic gas. Below the disk the movement of the H I-front is determined by the diffuse EUV radiation fields. After 10^4 yr (Fig. 2c) a clear head-tail configuration has developed. The head of the object has reached a quasi-steady state discussed below. At this point in time the tail is still evolving and has attained a length Z_{tail} greater than the extension of the numerical grid.

The middle row of Figure 2 shows the tail evolution after the H I-front has closed on the numerical grid. Evaporated material from the back side of the disk and redirected material from the head accumulates in the tip of the tail leading to a broad tail end (Fig. 2d). Induced by instabilities at the H I-front a globule of warm PDR material breaks off from the tail (Fig. 2e). The instabilities arise because the thin ionized gas compresses a denser and cooler gas (Rayleigh-Taylor instability) and because of the tangential velocities at the PDR side of the H I-front (Kelvin-Helmholtz instability). The instabilities cause wave-like disturbances in the H I-front which are recognizable at all times. In Figure 2f the object is displayed shortly after the globule left the computational domain with the evaporating flow. Again material accumulates in the tip of the tail. The periodic departing of globules in simulation A occurs a few times between $t = 2 \times 10^4$ yr and $t = 7 \times 10^4$ yr. The globules have masses $< 10^{-5} M_\odot$ and evaporate in less than 10^3 yr. These processes may explain the observed irregularities at the tail tips of the Orion proplyds.

The long-term evolution of the head-tail object is shown in frames g-i of Figure 2. The object maintains its general form but shrinks considerably. Figure 3 shows this behavior more quantitatively. The evolution of the radial extent of the C I-front R_C and of the H I-front R_H in the equatorial plane and the total length of the object in the Z -direction ($Z_{\text{head}} - Z_{\text{tail}}$) are shown as solid lines. Over the course of 13×10^4 yr the radius of the disk R_C has decreased from initially ~ 1000 AU to 80 AU. The decrease of $R_H \sim 2...4 \times R_C$ is less steep. The ratio of the total length in the Z -direction to the total width of the object $(Z_{\text{head}} - Z_{\text{tail}})/2R_H$ evolves from ~ 4 to ~ 3 . At the end of the evolution (Fig. 2i) the object has an H I-front width $2R_H = 560$ AU and length ~ 1600 AU. Due to the exponential decrease of R_C the evolution of the mass of the disk exhibits a similar behavior (Fig. 4, *solid line*). The time in which the disk mass shrinks to $1/e$ of its initial value is the evap-

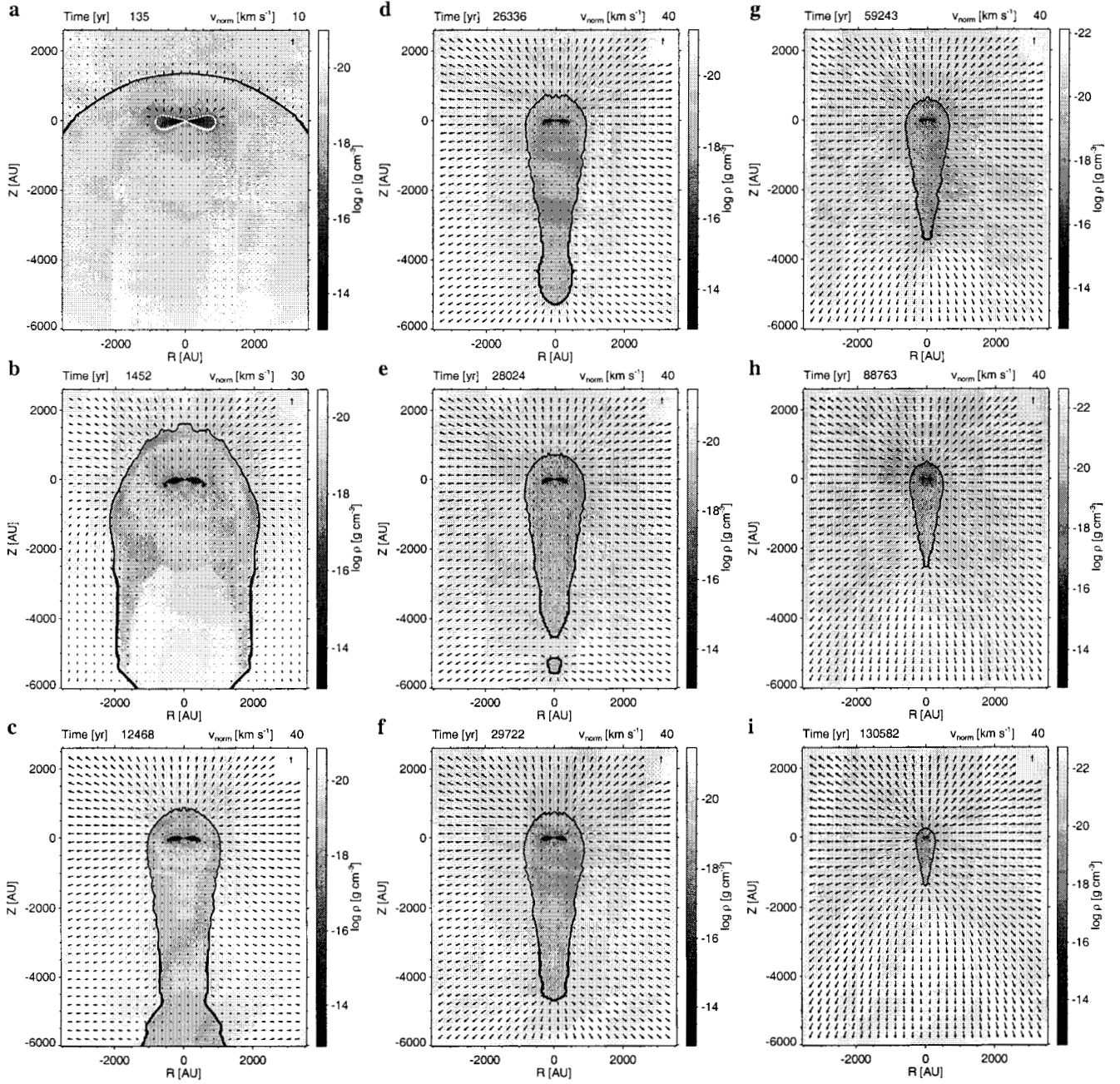


Fig. 2.— Evolution of star-disk system I under the influence of an external EUV and FUV radiation field (case A). The grey scale represents the density structure and the arrows the velocity field. The black lines are contour lines of constant degree of ionization of hydrogen and are given for $x = 0.2, 0.4, 0.6$, and 0.8 . Their concentration shows that the H I-front is indeed a discontinuity. The white lines in the first picture are contour lines of constant degree of ionization of carbon x_C and are given for the same values as for x , thus illustrating the C I-front discontinuity. For clarity these contours are not shown at later evolutionary times.

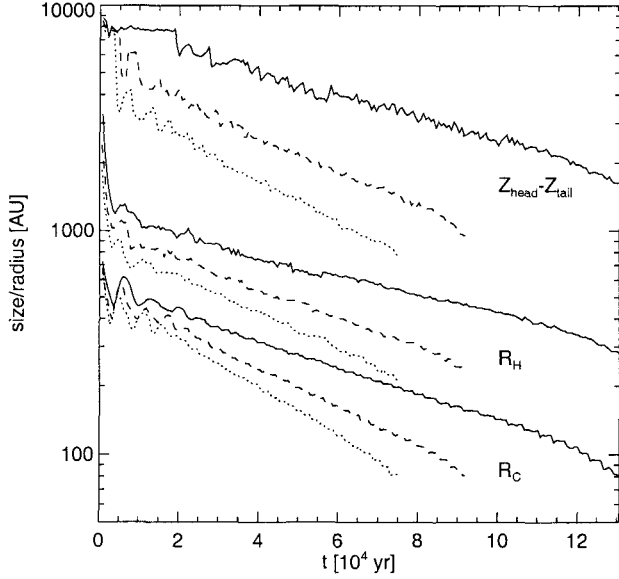


Fig. 3.— Evolution of the size of the head-tail object in Z -direction ($Z_{\text{head}} - Z_{\text{tail}}$), the radial width of the H I-front R_H and the radial width of the C I-front R_C at the equatorial plane for simulation A (solid lines), B (dashed lines), and C (dotted lines).

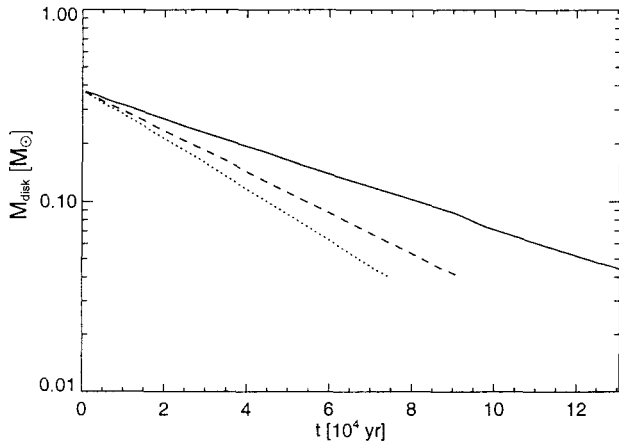


Fig. 4.— Evolution of the disk mass M_{disk} in simulation A (solid line), B (dashed line), and C (dotted line).

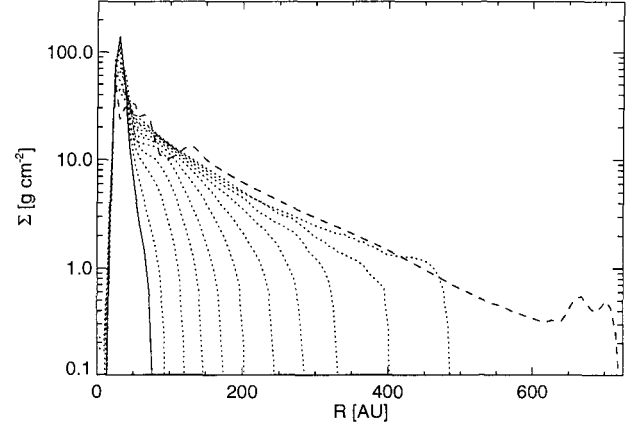


Fig. 5.— Evolution of the surface density Σ in simulation A. Σ is given near the beginning of the simulation (dashed lines, $t = 720$ yr), at the end of the simulation (solid line, $t = 13 \times 10^4$ yr) and at several intermediate stages (dotted lines, $\Delta t \sim 1.3 \times 10^4$ yr).

oration time scale $t_{\text{evap}} = 6.1 \times 10^4$ yr. The evolution of the surface density of the disk is displayed in Figure 5. The disk is photoevaporated from the outside in. The outer parts of the disk are more strongly affected than the central parts; the slope of the surface density increases during the evolution.

In Figure 6 the head of the object in simulation A at $t = 59\,243$ yr (Fig. 2g) is displayed in greater detail. The C I-front (white contour lines) tightly envelops the cool disk material ($T < 100$ K). The PDR between the C I-front and the H I-front shows the structure of a FUV-dominated flow as described by Störzer & Hollenbach (1999): A shock front separates the freely expanding neutral flow from a thick subsonic layer. The neutral flow accelerates due to pressure gradients and reaches velocities of $v_{\text{max}} = 10 \text{ km s}^{-1}$ before it is shocked. The density and gas temperature in the subsonic layer behind the shock front is fairly constant in the direction of the flow. Assuming momentum conservation in a spherically symmetric flow and a D-critical H I-front, the position of the shock front R_S can be calculated from

$$\frac{R_S}{R_H} = \sqrt{\frac{v_{\text{max}}}{2c_{\text{HII}}}} \sim 0.7, \quad (15)$$

where c_{HII} is the sound speed within the HII region (Johnstone et al. 1998). This result is in good agreement for the position of the shock front above and at the edge of the disk. In the subsonic layer material is

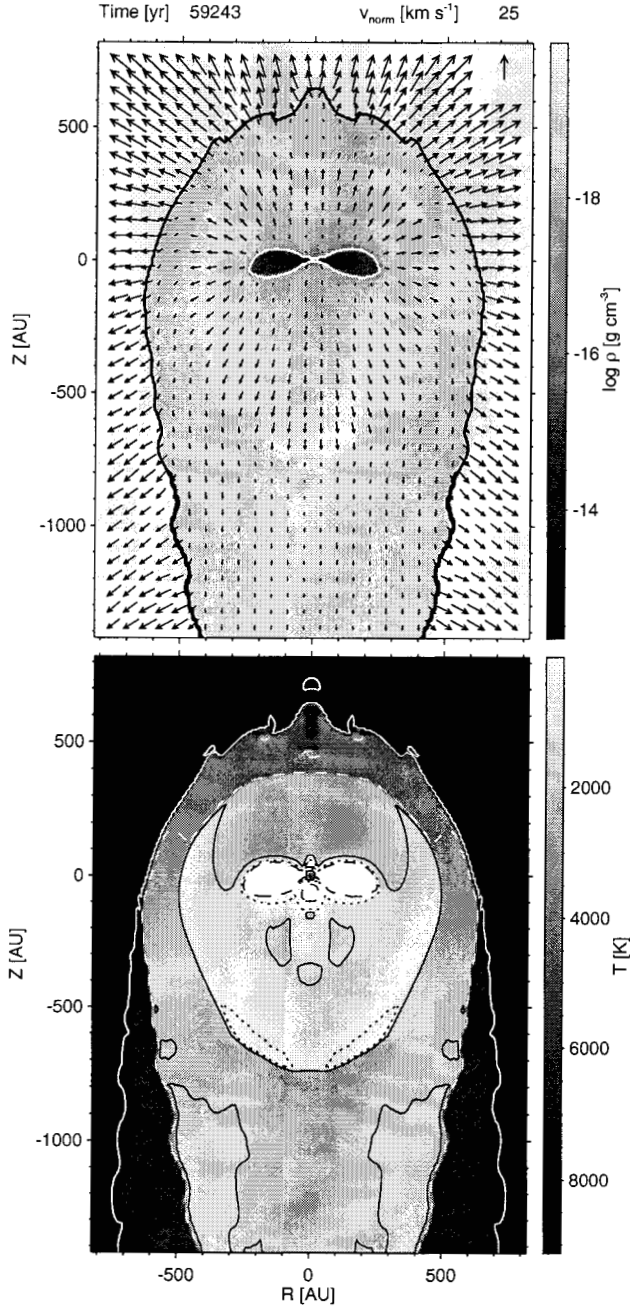


Fig. 6.— Head of the object in case A at $t = 59\,243$ yr (Fig. 2g). Top: Density, velocity, and degree of ionization of hydrogen and carbon. Bottom: Gas temperature T . The contour lines correspond to $T = 500$ K (black dashed), 1000 K (black dotted), 2000 K (black solid), 4000 K (white dashed), and 8000 K (white solid).

redirected from the head into the tail. The redirection rate in the equatorial plane is of order $10^{-7} M_{\odot} \text{ yr}^{-1}$ and fairly constant in time. Due to the redirection both the density and gas temperature within the subsonic layer decreases from above the disk to the edge of the disk. The radius of the shock front below the disk and the tail length are determined by the diffuse UV fields.

5.2. Influence of UV flux (B and C)

For cases B ($d = 0.05$ pc) and C ($d = 0.034$ pc) the distance between the circumstellar disk and the external star is smaller than for case A ($d = 0.1$ pc) but the evolution is very similar. The main difference is a more rapid evolution of the tail because of the more intense EUV fields. Departing neutral globules were not recognizable in the data sets sampled every ~ 700 yr. Figure 7 displays the head-tail objects in simulations A, B, and C at evolutionary times for which the disk radii R_C are approximately equal. With decreasing distance the thickness of the neutral layer, the radius of the H I-front R_H , and the size of the object ($Z_{\text{head}} - Z_{\text{tail}}$) decrease (see also Fig. 3). For cases B and C the mass of the disk decreases more rapidly than for case A (Fig. 4). The corresponding values for the evaporation time scale t_{evap} are given in Table 3.

The flow within the PDR head is a FUV-dominated flow for all times in all cases. For a dust extinction coefficient $\sigma^{\text{ext}} = 8 \times 10^{-22} \text{ cm}^2$ and a preshock velocity $v_{\text{max}} = 3 \text{ km s}^{-1}$ Störzer & Hollenbach (1999) predict FUV-dominated flows for FUV fluxes in the range of $5 \times 10^4 < G_0 < 2 \times 10^7$ and disk radii between $10 \text{ AU} < R_C < 100 \text{ AU}$. For higher v_{max} and

Table 3: Parameter fits for Photoevaporation Rates

case	t_{evap} 10^4 yr	\dot{M}_{100} $10^{-6} M_{\odot} \text{ yr}^{-1}$	δ
A	6.1	0.70	1.32
B	4.1	1.16	1.27
C	3.3	1.55	1.23

Note— t_{evap} = evaporation time scale; \dot{M}_{100} & δ : results of a power law fit of the form $\dot{M}_{\text{ph}} = \dot{M}_{100} (R_C/100 \text{ AU})^{\delta}$ for the dependence of the photoevaporation rate \dot{M}_{ph} on the radius of the C I-front.

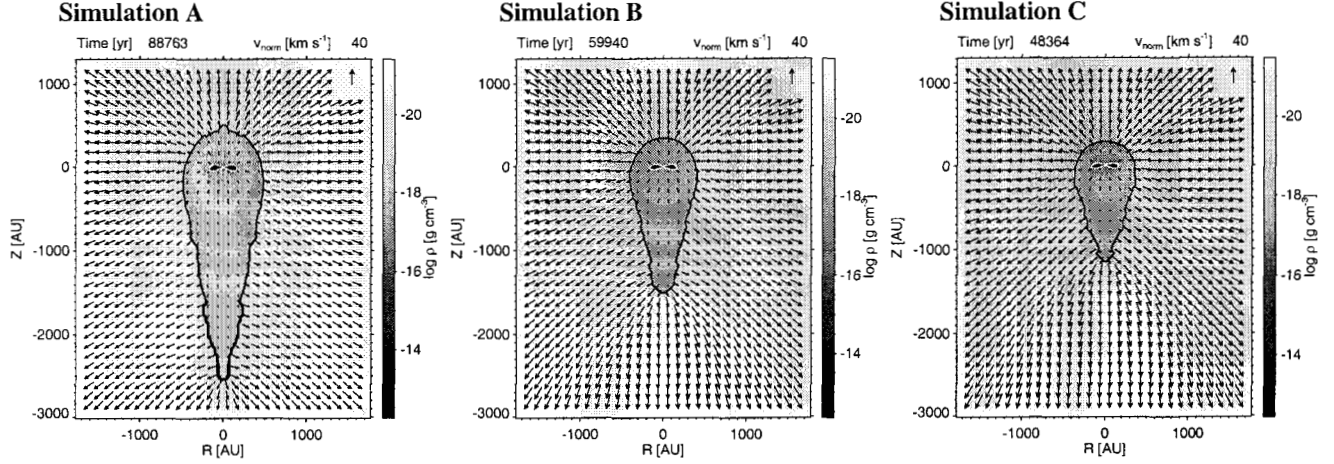


Fig. 7.— Density and velocity structure of the head-tail objects in simulations A, B, and C at evolutionary times when the radius of the disk R_C is equal in all three cases.

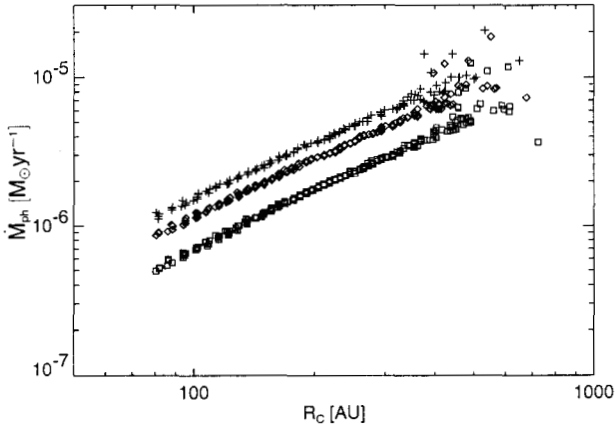


Fig. 8.— Photoevaporation rate \dot{M}_{ph} as a function of the radius of the C I-front R_C for case A (*squares*), case B (*diamonds*) and case C (*crosses*).

for lower σ^{ext} FUV-dominated flows are possible for much larger R_C . These results are compatible with our simulations: We use a dust extinction coefficient $\sigma^{\text{ext}} = 5 \times 10^{-22} \text{ cm}^2$, calculate preshock velocities $v_{\text{max}} \approx 10 \text{ km s}^{-1}$, and obtain FUV-dominated flows for disks with radii of several 100 AU. In our simulations the FUV fluxes are in the range $10^5 < G_0 < 10^6$.

The dependence of the photoevaporation rate \dot{M}_{ph} on the radius of the disk R_C is shown in Figure 8 for case A, B, and C. According to Johnstone et al. (1998) \dot{M}_{ph} is given by the density n_0 and the flow speed v_0 at the base of the flow integrated over a spherical clump with radius r_0

$$\dot{M}_{\text{ph}} = 4\pi r_0^2 n_0 v_0 \quad (16)$$

In FUV-dominated flows the optical depth is dominated by dust extinction $\tau_{\text{FUV}} \sim \int \sigma_{\text{ext}} n \, ds$. In this case the gas column density in the PDR $N_{\text{H}} \sim 1/\sigma_{\text{ext}}$ for $\tau \sim 1$. If the supersonic flow region dominates the column density, then $N_{\text{H}} \sim n_0 r_0$ and $\dot{M}_{\text{ph}} \propto r_0$. Fitting the numerical results to a power law of the form

$$\dot{M}_{\text{ph}} = \dot{M}_{100} \left(\frac{R_C}{100 \text{ AU}} \right)^\delta, \quad (17)$$

yields an exponent $\delta = 1.23 - 1.32$ (Tab. 3) which is in agreement with the results of Störzer & Hollenbach (1999), who find $\dot{M} \sim 10^{-7} \text{ M}_\odot \text{ yr}^{-1} (r_0/100 \text{ AU})^{1-1.5}$ for $d \approx 0.2 \text{ pc}$ (Hollenbach et al. 2000). In our simulations the value of \dot{M}_{100} is almost an order of magnitude higher because d and σ_{ext} are lower. Also, the

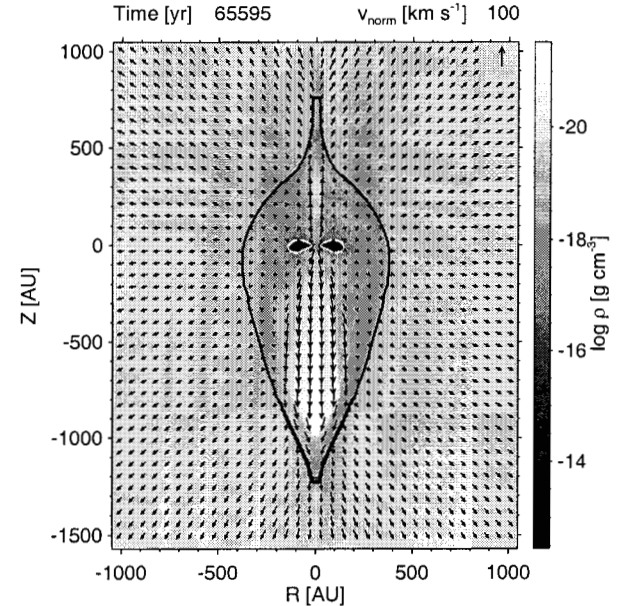
neutral subsonic layer contributes significantly to the total column density. Due to redirection of material from the head into the tail this contribution is smaller at the edge of the disk, leading to a higher value for n_0 and consequently to a higher value for \dot{M}_{ph} .

The size of the objects at the end of the simulations (see Fig. 3) are comparable to the observations. The proplyds in the Orion Nebula have H I-front widths between 44 AU and 1720 AU and lengths between 200 AU and 1600 AU. The ratio of the H I-front radius divided by the semi-major axis of the dark silhouette ranges from about 1.5 to 4 (Bally et al. 1998a). Disk masses derived from observations at 1.3 mm (Bally et al. 1998b) yield $M_{\text{disk}} \lesssim 0.02 M_{\odot}$. In the simulations the mass of the disk would reach this limit after $t \gtrsim 10^5$ yr. Since the disks are assumed to be on circular orbits ($d = \text{const}$) and are always illuminated face-on, the calculated evaporation time scales t_{evap} are lower limits. Hence, the results are consistent with an illumination time scale of no more than $\sim 10^6$ yr, the estimated age of θ^1 Ori C.

5.3. Influence of stellar wind (case D and E)

Simulations D and E start with the model of case A at $t = 59.3 \times 10^3$ yr (Fig. 2g). For case D the stellar wind velocity is gradually increased to a velocity $v_{\text{wind}} = 100 \text{ km s}^{-1}$ and for case E to $v_{\text{wind}} = 200 \text{ km s}^{-1}$. In Figure 9 the structure of the models is displayed after a quasi-steady state flow has been established. In both cases the spherically symmetrical wind emerging from the central protostar is collimated within the PDR to a bipolar outflow by the ram pressure of the neutral evaporating flow $(v\dot{M})_{\text{ph}}$. The opening angle of the jet is proportional to the ratio $(v\dot{M})_{\text{wind}}/(v\dot{M})_{\text{ph}}$ (Yorke & Welz 1996). Since \dot{M}_{ph} is smaller below the disk the opening angle is greater than above the disk. The disk itself and the location of the C I-front are not effected but the shape of the H I-front is modified by the more powerful stellar winds. Above the disk the ram pressure of the jet $(v\dot{M})_{\text{wind}}$ is able to push the H I-front near the rotation axis toward the ionizing star. For case D $(v\dot{M})_{\text{wind}}$ is too low to change the structure of the H I-front of the tail significantly, whereas for case E the jet breaks through and the low-density wind region becomes completely ionized.

Simulation D



Simulation E

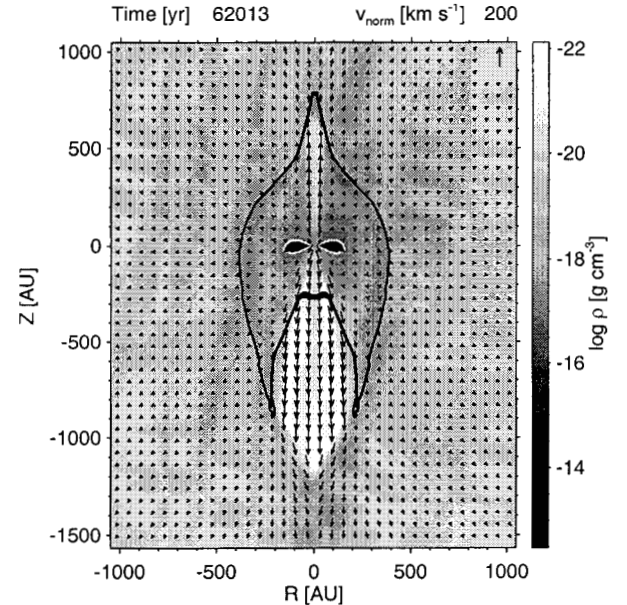


Fig. 9.— Density and velocity structure of the model at the end of simulation D ($v_{\text{wind}} = 100 \text{ km s}^{-1}$) and E ($v_{\text{wind}} = 200 \text{ km s}^{-1}$). The mass loss rate of the stellar wind is $\dot{M}_{\text{wind}} = 2 \times 10^{-7} M_{\odot} \text{ yr}^{-1}$ in both cases.

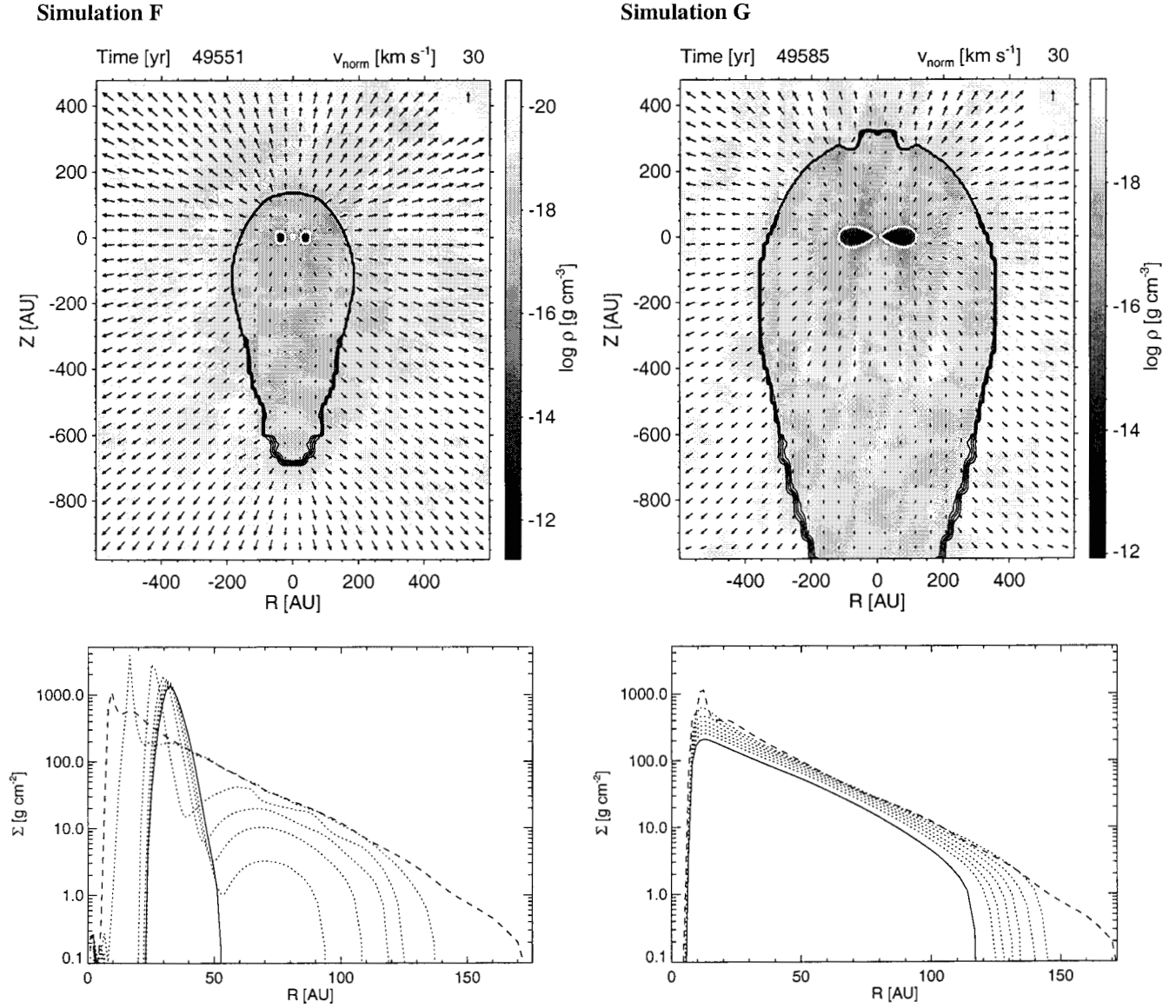


Fig. 10.— Density, I-front, and velocity structure (top) and the corresponding evolution of the surface density Σ (bottom) at the end of the simulations F (negligible angular momentum transport) and G (significant angular momentum transport). Σ is given near the begin of the simulation (*dashed lines*, $t \lesssim 100$ yr), at the end of the simulation (*solid lines*, $t = 5 \times 10^4$ yr), and at several intermediate stages (*dotted lines*, $\Delta t \sim 6 \times 10^3$ yr).

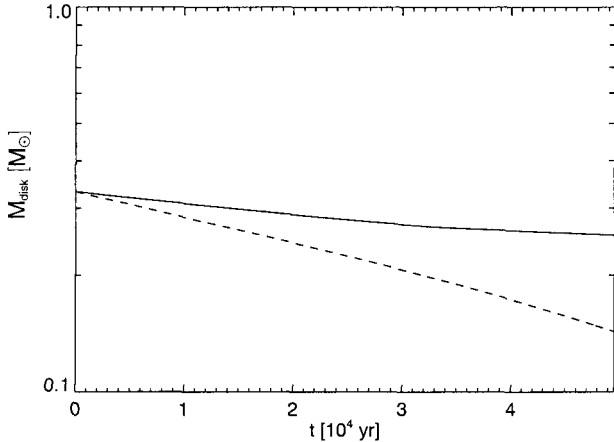


Fig. 11.— Evolution of the disk mass in simulation F (solid line) and G (dotted line).

5.4. Influence of angular momentum transfer (case F and G)

With simulation F and G we examine the importance of angular momentum transfer for the evolution of externally illuminated disks. We model angular momentum transfer according to an α formalism (Shakura & Sunyaev 1973): the kinematic viscosity coefficient is given by $\nu = \alpha c_s H$, where α is a dimensionless parameter, c_s the sound speed, and H the scale height of the disk. We begin these simulations with star-disk model II. The collapse simulations associated with this initial configuration implicitly assume that angular momentum transport is initiated by tidal forces due to gravitational instabilities and α is adjusted according to the value of the Toomre parameter (Yorke & Bodenheimer 1999). In contrast to model I the compact disk of model II is more unstable against non-axisymmetric gravitational modes leading to a higher α and therefore to a higher accretion luminosity (see L_{star} in Tab. 1). Here, we do not attempt to model a particular mechanism for the transport of angular momentum but assume a constant value for α for two extreme cases: Case F is a simulation with negligible angular momentum transfer ($\alpha = 10^{-6}$) and for case G we use $\alpha = 10^{-2}$. All other parameters are the same as for case B.

The results of both cases are shown in Figure 10. We compare the simulations at the same evolutionary times at the end of the calculations. The upper pictures show the density and velocity structure and the lower pictures the evolution of the surface den-

sity. In both cases the size of the ionized envelope is comparable to the observations even at very early stages. In case F the disk completely changes its internal structure because of the sudden decrease of angular momentum transfer. The final structure is that of a torus. Due to the low disk surface the mass of the disk decreases very slowly (Fig. 11). The evaporation time scale in case F is $t_{\text{evap}}^{\text{F}} = 18 \times 10^4$ yr. In case G the disk maintains its structure. As in case B the disk is photoevaporated from outside, but the slope of the surface density remains the same. The photoevaporation time scale $t_{\text{evap}}^{\text{G}} = 6.1 \times 10^4$ yr is about 3 times shorter than in case F. Thus, it is necessary to know the efficiency of angular momentum transport mechanisms to determine the lifetime of a disk in an external radiation field properly.

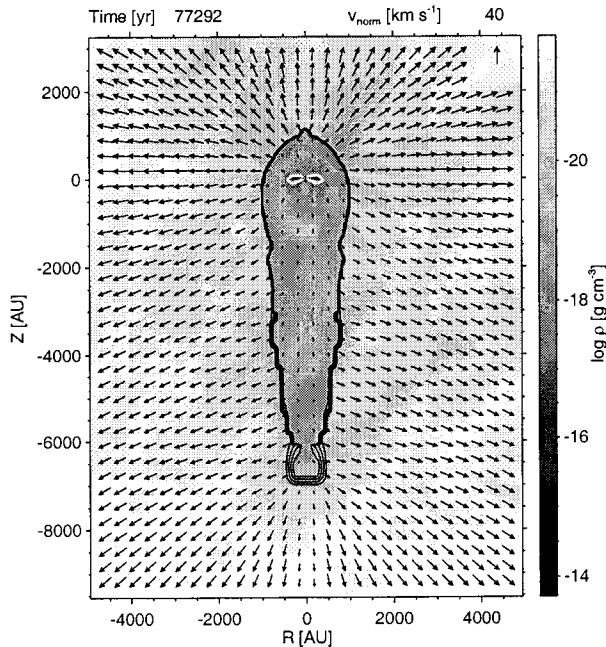
The torus-shaped disk at the end of simulation F resulting from a sudden change of α may have no direct counterpart in nature. However, it could be considered as an example for a disk whose inner regions are cleared by a close companion analogous to the circumbinary disk of GG Tau (Guilloteau, Dutrey & Simon 1999). Our simulations thus predict that circumbinary disks are *less* susceptible to destruction by photoevaporation than circumstellar disks, i.e., their photoevaporation time scales are longer.

5.5. Influence of the FUV/EUV ratio (case H and J)

Simulations H and J begin with star-disk model III. The initial conditions are the same for both cases except that the FUV/EUV ratio is 5 times higher for case J than for case H (Tab. 2). Figure 12 shows a comparison of the head-tail objects at evolutionary times with equal disk radii. For simulation J the wind-blown bubble within the PDR is greater than for case H and shows an elliptical shape. Moreover, the radius of the H I-front $R_{\text{H}} \sim 5 \times R_{\text{C}}$ and the tail length Z_{tail} are greater than for case H. The decrease in disk mass is faster for case J (Fig. 13). Accordingly, the corresponding photoevaporation time scale of case J ($t_{\text{evap}}^{\text{J}} = 4.8 \times 10^4$ yr) is shorter than for case H ($t_{\text{evap}}^{\text{H}} = 7.4 \times 10^4$ yr).

High FUV/EUV ratios are to be expected. Realistic models for stellar atmospheres (Pauldrach et al. 1998) result in FUV/EUV ratios for the cooler OB stars ($T_{\text{eff}} < 30\,000$ K) which are up to ten times higher than those calculated from equation 1 and 2 using Planck's function. In particular, this fact should

Simulation H



Simulation J

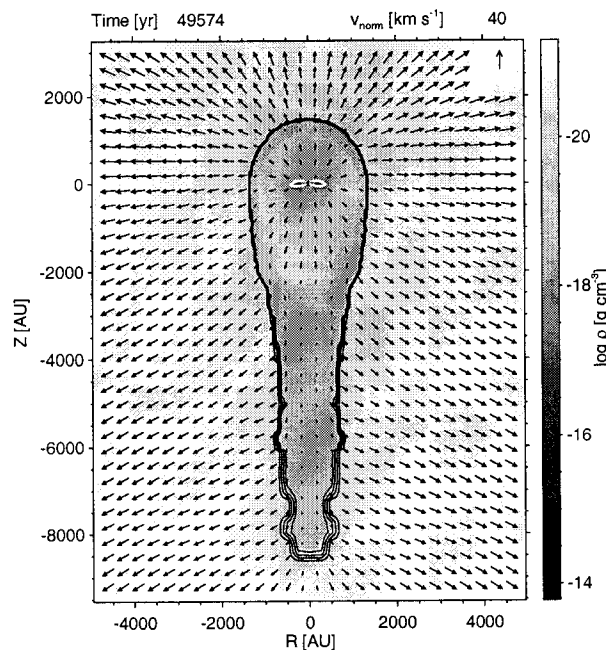


Fig. 12.— Density and velocity structure of the head-tail objects in simulations H and J at evolutionary times for which the disk radius R_C is the same.

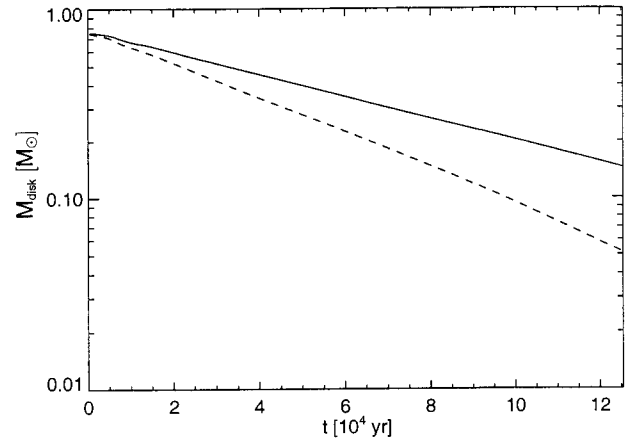


Fig. 13.— Evolution of the disk mass in simulation H (*solid line*) and J (*dotted line*).

have impacts on star-disk systems in the vicinity of OB clusters where less massive members provide an FUV photon excess. The FUV/EUV ratio could also be enhanced due to the increasing UV dust extinction coefficient κ^{ext} with photon energy. This effect is not considered in the simulations because the absolute value of κ^{ext} strongly depends on the dust model (Preibisch et al. 1993). Some of the Orion Nebula proplyds have large $R_H \sim 4 \times R_C$ (Bally et al. 1998a). This is not necessarily a strong indication of a high FUV/EUV ratio in the Trapezium Cluster, because R_H/R_C is also large for smaller values of R_C and larger distances to the ionizing source (see 5.2).

6. Emission line maps

For direct comparison with observations we use a ray-tracing code to calculate line spectra and emission line maps. The basic features of this code optimized for circumstellar disks embedded in an ionized medium are described in Kessel, Yorke & Richling (1998). For the present investigation we use a modified version especially adapted to the case of externally illuminated disks. We examine the optical lines [OIII] 5007 Å, [OII] 3726 Å, H α , [NII] 6584 Å, and the NIR lines [OI] 63 μm and [CII] 158 μm .

Before the actual ray-tracing procedure the abundances of OII, OIII, and NII are determined by solving the equation for ionization and recombination balance. The degree of ionization of hydrogen and carbon are known. For the NIR lines it is assumed that there is no contribution to the emission in regions

where hydrogen is ionized. Then the code solves the rate equations to obtain the population density for the upper level n_i . The line emissivity for a transition from level i to level j is calculated from

$$\epsilon = \frac{1}{4\pi} n_i A_{ij} h\nu_{ij} \beta_{\text{esc}}(\tau_{ij}), \quad (18)$$

where A_{ij} is the spontaneous transition probability and $h\nu_{ij}$ the energy difference between level i and j . The escape probability β_{esc} is only considered for the NIR lines. The ray-tracing code itself solves the time-independent equation of radiation transfer for a non-relativistic moving medium along lines of sight for different viewing angles. The resulting emission line maps are convolved with a Gaussian point spread function with a FWHM of 22 AU, which is comparable to the resolution of the HST for the distance of the Orion Nebula.

Figure 14 shows the emissivity ϵ and the calculated line profiles for case A at $t = 59\,243$ yr shown in Figure 2g. In addition, for the forbidden lines of OII, OIII, and NII contour lines for the relevant degrees of ionization are given. The abundance of OII is high near the H I-front and in the shadow regions ionized by diffuse EUV photons. Further outside in regions ionized by direct EUV photons OII becomes ionized and the abundance of OIII increases. The emissivity of [OIII] 5007 is thus more extended than the emissivity of [OII] 3726. The emissivity of H α and [NII] 6584 is similar to that of [OII] 3726. They attain their maxima at the H I-front. The degree of ionization of NII falls off more rapidly than the degree of ionization of OII because the ionization potential of NII is lower than the ionization potential of OII. The emissivity of the NIR lines is strongest at the C I-front near the disk surface and in the compressed subsonic PDR regions beyond the wind-blown cavity.

The line profiles in Figure 14 are given for five different viewing angles. The viewing angle is defined as the angle between the rotation axis of the disk and the line of sight. A viewing angle of 0° means we observe the disk pole-on from the direction of the ionizing star. At a viewing angle of 90° the disk is observed edge-on. The line profiles mirror the velocity field of the ionized and neutral material. Depending on the viewing angle the forbidden lines have maxima at the blue or red wing between 5 and 20 km/s. This is most clearly visible in the [OIII] line, since part of the emission comes from the accelerated ionized gas further away from the H I-front. These results

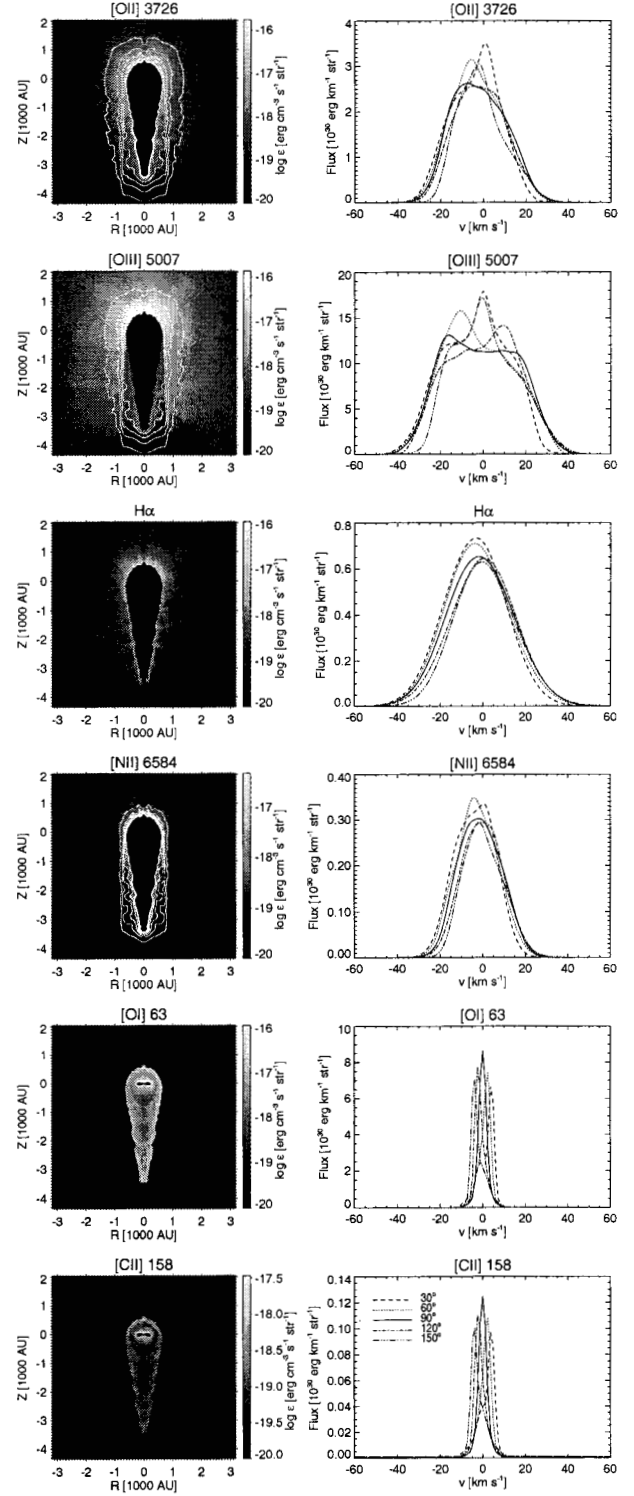


Fig. 14.— Emissivity and line profiles for the model at $t = 59\,243$ yr in simulation A (Fig. 2g). The contour lines of the relevant degree of ionization are given for the values 0.2, 0.4, 0.6, and 0.8.

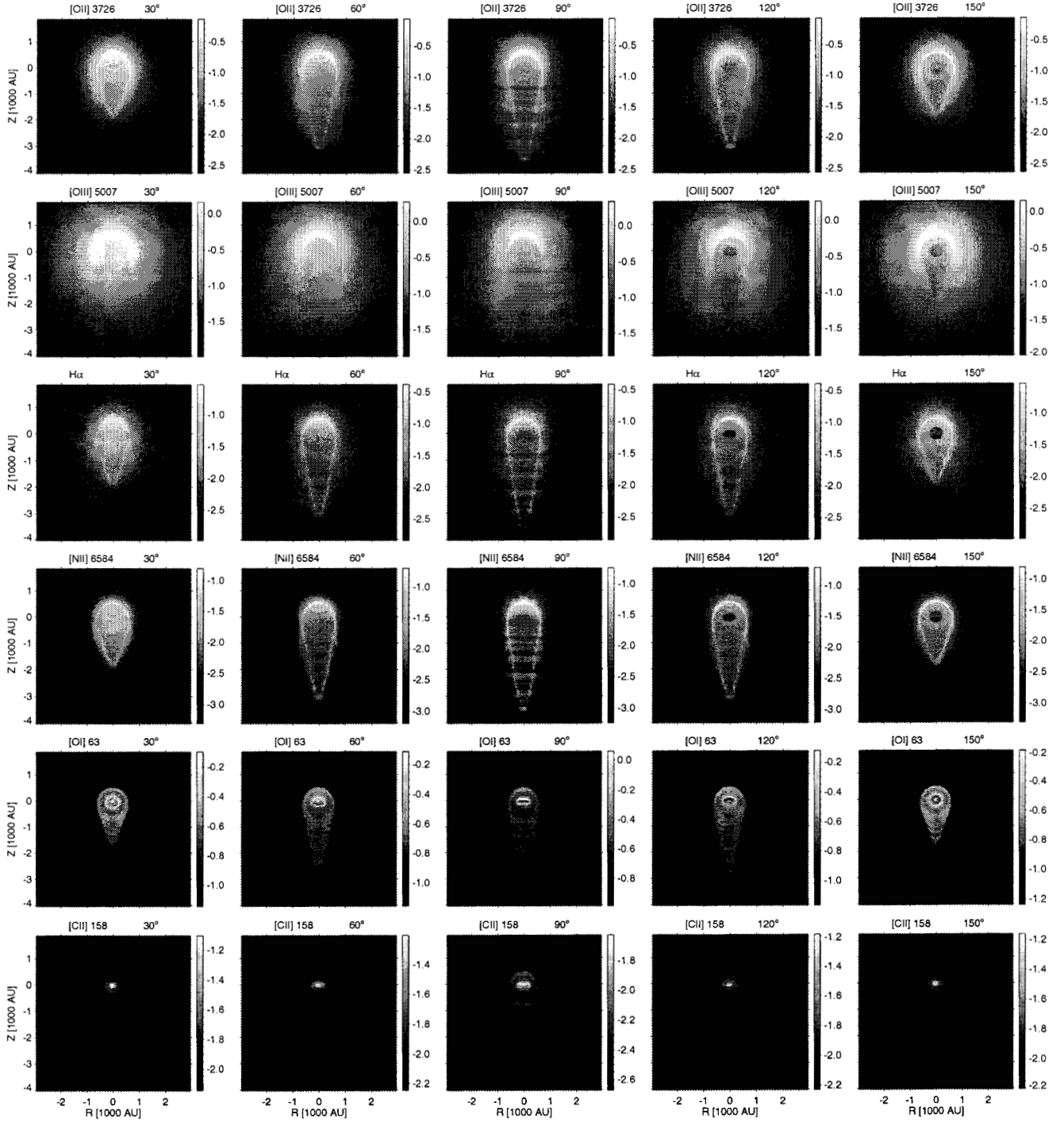


Fig. 15.— Emission line maps for the model at $t = 59243$ yr in simulation A (Fig. 2g) for five different viewing angles. The intensity is given in $\log(I/\text{erg s}^{-1} \text{cm}^{-2} \text{str}^{-1})$.

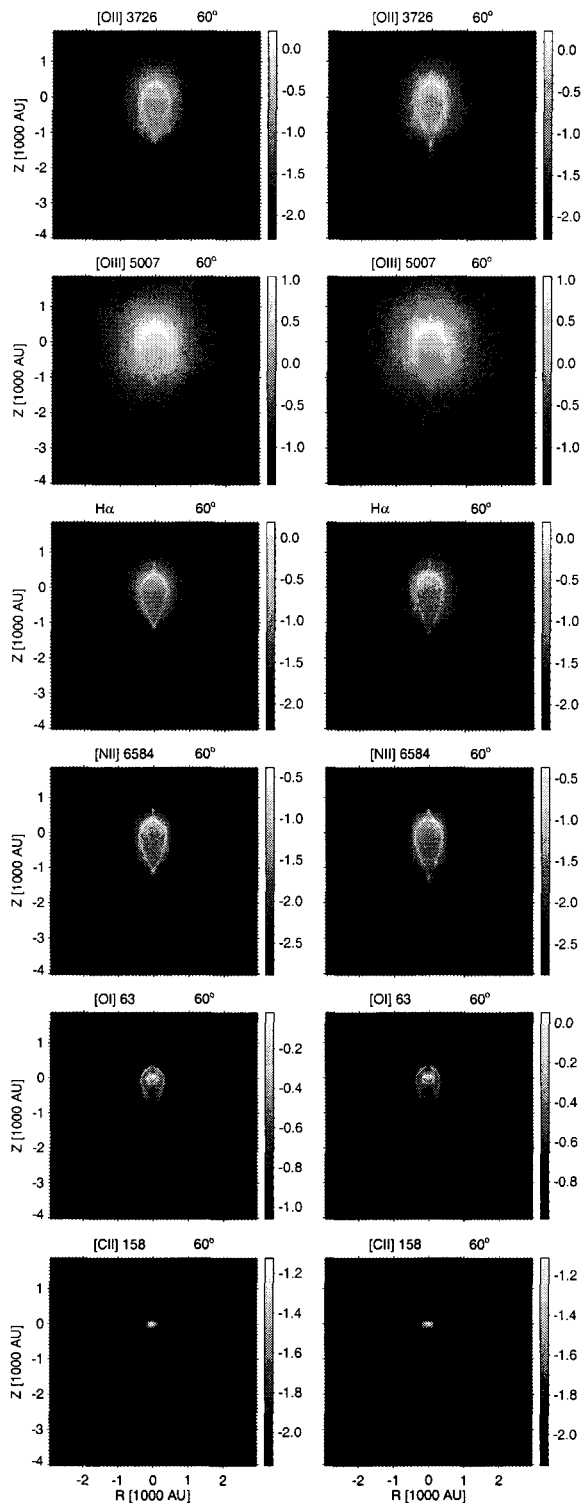


Fig. 16.— Emission line maps for the final models of case D (*right*) and E (*left*) shown in Fig. 9.

are consistent with the high resolution spectroscopy of four proplyds in the Orion Nebula by Henney & O'Dell (1999) who find a clear correlation of spectral line width with ionization potential. Due to the low atomic weight of hydrogen the broad $H\alpha$ line shows the least variation with viewing angle. The NIR lines are much narrower because they mainly trace the low velocity material near the disk surface and in the sub-sonic regions.

In Figure 15 the corresponding emission line maps are displayed. As expected from the emissivity distributions shown in Figure 14, the emission line maps of [OII], $H\alpha$, and [NII] are quite similar. The emission is brightest at the head of the object and along of the tails and is thus consistent with observations which show limb-brightened tails (Bally et al. 1998a). For viewing angles $\gtrsim 90^\circ$ a silhouette disk is visible in the bright envelope. The [OIII] maps show more diffuse emission line crescents. For angles $\lesssim 60^\circ$ the emission is very weak in the direction of the tail. Here, for angles $\gtrsim 60^\circ$ the silhouette disk already becomes visible. For viewing angles $\gtrsim 90^\circ$ the tail is in absorption against the diffuse emission. These results are also consistent with the observations by Bally et al. (1998a). The last two rows of Figure 15 are the emission line maps of the NIR lines [OI] and [CII]. They show the strong emission of the warm PDR gas at the disk surface and the fainter emission between the H and C I-front. Although it is not yet possible to observe these lines, they will provide an important diagnostic tool for interpreting the PDRs associated with photoevaporation disks.

Figure 15 shows the emission line maps for the models with the faster stellar winds (case D and E, see Fig. 9). The narrow extension of the H I-front toward the ionizing source is clearly visible in the optical lines. Only for case E where the wind is strong enough to break through the H I-front can the counter-jet be observed. In the NIR lines the emission in the tail is no longer visible due to the low density in the fast wind region. Stellar winds emerging from the central objects of the Orion Nebula proplyds are apparently not very powerful, since their micro-jets are mostly monopolar (Bally et al. 1999).

7. Conclusions

Our improved radiation hydrodynamics code is able to realistically describe the photoevaporation of circumstellar disks illuminated by external EUV and

FUV sources. Despite the simplified PDR physics employed here, our results are consistent with the more elaborate PDR models by Störzer & Hollenbach (1999). In contrast to these PDR models we find several new features that are intrinsic to our self-consistent multidimensional approach.

The results of the simulations confirm that the photoevaporating disk model can explain most of the observed features of the Orion Nebula proplyds and proplyds in M8, NGC 2024, and NGC 3603. The interaction of the FUV-induced neutral flow at the disk surface with the direct and diffuse EUV radiation fields leads to the typical head-tail objects with bright emission line crescents and tails pointing away from the external radiation source. After being illuminated for times $\gtrsim 10^5$ yr, the initially rather massive disks we employ as starting models attain the masses typically observed. At this time the radius of the disk, the radius of the H I-front and the length of the tail are comparable to the observations. This is a strong indication that inferred masses and radii of observed disks significantly underestimate their values during earlier evolutionary phases and is consistent with the results of Yorke & Bodenheimer (1999) that immediately after disk formation the ratio of disk mass to star mass can be as high as 1:3 and disk radii can exceed 1000 AU.

Circumstellar disks are not necessarily seen as silhouettes in the emission line maps of proplyds, since their observability depends strongly on their orientation with respect to the ionizing sources and the observer. The [OIII] emission appears more diffuse than the other emission lines considered, because the relative abundance of OIII is low in the compressed regions e.g. near the H I-front and in the shadow regions along the tail.

Monopolar and bipolar micro-jets emerging from the proplyds can be explained by spherically symmetric stellar winds focused by the neutral evaporating flow from the disk surface. Because of the symmetry assumed, these micro-jets necessarily coincide with the head-tail orientation of our simulated proplyds. With a more elaborate 3D treatment a more complex flow pattern of focussed stellar winds and photoevaporation outflows will result.

If sufficient angular momentum transfer is present, the evaporation time scale is almost independent of the initial radius of the disk and consequently of the compactness of the parental molecular cloud cores. Note that this does not necessarily mean that the life-

time of protostellar disks is independent of the compactness of the cluster within which it formed (see below).

Due to our assumed face-on illumination and the fixed distance to the illuminating star the calculated evaporation time scales yield an lower limit for the illumination time scale 10^5 yr which lies in the range of the observed age of the Trapezium Cluster. The evaporation time scale is influenced by angular momentum transfer and the FUV/EUV flux ratio. Within the parameter space investigated here, either mechanism can change the evaporation time scale by a factor of 2 to 3. Tidal stripping by close or penetrating encounters (Hall 1997) as well as inner disk clearing by close companions steepen the surface density profile and actually lead to more robust disks and longer evaporation time scales. In the dense Trapezium Cluster where $n_{\text{core}} = 2 \times 10^4$ stars pc^{-3} (Hillenbrand & Hartmann 1998) both effects can be expected, assuming a binary fraction comparable to the galactic field (Petr et al. 1998). Further investigations are planned to consider orbital data obtained by N-body simulations of cluster evolution scenarios (Kroupa, Petr & McCaughrean 1999)

This research has been supported by the Deutsche Forschungsgemeinschaft (DFG) within the framework of the “Physics of Star Formation” program under grant Yo 5/19-2 and by the National Aeronautics and Space Administration (NASA) under the auspices of the “Origins” Program. Portions of this research were conducted at Jet Propulsion Laboratory, California Institute of Technology. The calculations were performed at the John von Neumann Institute for Computing (NIC) in Jülich and the Leibniz Computing Center (LRZ) in Munich.

REFERENCES

- Bakes, E.L.O., Tielens, A.G.G.M. 1994, *ApJ*, 427, 822
- Bally, J., Sutherland, R.S., Devine, D., Johnstone, D. 1998a, *AJ*, 116, 293
- Bally, J., Testi, L., Sargent, A., Carlstrom, J. 1998b, *AJ*, 116, 854
- Bally, J., O’Dell, C.R., McCaughrean, M., Sutherland, R.S. 1999, *AAS*, 194, 6812b
- Bertoldi, F. 1999, *A&A*, in press

- Brandner, W., Grebel, E.K., Chu, Y.-H., Richling, S., Yorke, H.W., Dottori, H., Monetti, A., Zinnecker, H., Points, S.D. 1999, AAS 194, 6808b
- Cesaroni, R., Felli, M., Jenness, T., Neri, R., Olmi, L., Robberto, M., Testi, L., Walmsley, C.M. 1999, A&A 345, 949
- Chen, H., Bally, J., O'Dell, C.R., McCaughrean, M.J., Thompson, R.L., Rieke, M., Schneider, G., Young, E.T. 1998, ApJ, 492, L173
- Close, L.M., Dutrey, A., Roddier, F., Guilloteau, S., Roddier, C., Northcott, M., Menard, F., Duvert, G., Graves, J.E., Potter, D. 1998 ApJ, 499, 883
- de Jong, T., Dalgarno, A., Boland, W. 1980, A&A, 91, 68
- Draine, B.T., Lee, H.M. 1984, ApJ, 285, 89.
- Guilloteau, S., Dutrey, A., Simon, M. 1999, A&A, in press
- Hall, S.M. 1997, MNRAS, 287, 148
- Henney, W.J., O'Dell, C.R. 1999, ApJ, in press
- Hillenbrand, L.A. 1997 AJ, 113, 1733
- Hillenbrand, L.A., Hartmann, L.W. 1998 ApJ, 492, 540
- Hollenbach, D., Tielens, A.G.G.M. 1997, ARA&A, 35, 179
- Hollenbach, D., Yorke, H.W., Johnstone, D. 2000, in Protostars & Planets IV, ed. V. Mannings, A.P. Boss & S.S. Russell (Tucson: University of Arizona Press), in press
- Johnstone, D., Bertoldi, F. 1998, in The Orion Complex Revisited, ASP Conference Series
- Johnstone, D., Hollenbach, D., Bally, J. 1998, ApJ, 449, 758
- Kessel, O., Yorke, H.W., Richling, S. 1998, A&A, 337, 882
- Körner, D.W., Ressler, M.E., Werner, M.W., Backman, D.E. 1998, ApJ 503, L83
- Kroupa, P., Petr, M.G., McCaughrean, M.J. 1999, NewA, in press
- Levermore, C., Pomraning, G. 1981, ApJ, 248, 321
- Mannings, V., Sargent, A.I. 1999, ApJ, in press
- McCaughrean, M.J., Stauffer, J.R. 1994, AJ, 108, 1382
- Nahar, S.N., Pradhan, A.K. 1994, Phys. Rev. A, 49, 1816
- O'Dell, C.R., Wen, Z., Hu, X. 1993, ApJ, 410, 696
- Padgett, D.L., Brandner, W., Stapelfeldt, K.R., Strom S.E., Terebey S., Körner, D. 1999, AJ, 117, 1490
- Pauldrach, A.W.A., Lennon, M., Hoffmann, T.L., Sellmaier, F., Kudritzki, R.-P., Puls, J. 1998, in ASP Conf. Ser., 131, Properties of Hot, Luminous Stars, ed. Ian Howarth, p. 258
- Petr, M.G., Du Foresto, V., Beckwith, S.V.W., Richichi, A., McCaughrean, M.J. 1998, ApJ, 500, 825
- Preibisch, Th., Ossenkopf, V., Yorke, H.W., Henning, Th. 1993, A&A, 279, 577.
- Richling, S., Yorke, H.W. 1997, A&A, 327, 317
- Richling, S., Yorke, H.W. 1998, A&A, 340, 508
- Shakura, N.I., Sunyaev, R.A. 1973, A&A, 24, 337
- Spaans, M., Tielens, A.G.G.M., van Dishoeck, E.F., Bakes, E.L.O. 1994, ApJ, 437, 270
- Stapelfeldt, K.R., Krist, J.E., Menard, F., Bouvier, J., Padgett, D.L., Burrows, C.J. 1998, ApJ, 502, L65
- Stapelfeldt, K.R., et al. 1999, in preparation
- Stecklum, B., Henning, T., Feldt, M., Hayward, T.L., Hoare, M.G., Hofner, P., Richter, S. 1998, AJ, 115, 767
- Sternberg, A. & Dalgarno, A. 1995, ApJS99, 565
- Störzer, H., Hollenbach, D. 1998, ApJ, 495, 853
- Störzer, H., Hollenbach, D. 1999, ApJ, 515, 669
- Suttner, G., Yorke, H.W., Lin, D.N.C., 1999, ApJ, 525, in press
- Tielens, A.G.G.M., Hollenbach, D. 1985, ApJ, 291, 722
- Yorke, H.W., Bodenheimer, P. 1999, ApJ, in press

Yorke, H.W., Kaisig, M. 1995, Comp. Phys. Comm.
89, 29

Yorke, H.W., Welz, A. 1996, A&A315, 555